Supplementary Information for

# Efficient tandem electroreduction of nitrate into ammonia through coupling Cu single atoms with adjacent $Co_3O_4$

Yan Liu[1,7], Jie Wei[1,7], Zhengwu Yang[1,7], Lirong Zheng[2,], Jiankang Zhao[1,], Zhimin Song[1,], Yuhan Zhou[1,], Jiajie Cheng[3,], Junyang Meng[1,], Zhigang Geng[1]*, Jie Zeng[1,4,5,6,]*

[1]Hefei National Research Center for Physical Sciences at the Microscale, University of Science and Technology of China, Hefei, Anhui 230026, P. R. China

[2]Institute of High Energy Physics, Chinese Academy of Sciences, Beijing 100049, P. R. China

[3]Department of Physics, University of Science and Technology of China, Hefei, Anhui 230026, P. R. China

[4]CAS Key Laboratory of Strongly-Coupled Quantum Matter Physics, University of Science and Technology of China, Hefei, Anhui 230026, P. R. China

[5]Key Laboratory of Surface and Interface Chemistry and Energy Catalysis of Anhui Higher Education Institutes, Department of Chemical Physics, University of Science and Technology of China, Hefei, Anhui 230026, P. R. China

[6]School of Chemistry & Chemical Engineering, Anhui University of Technology, Ma'anshan, Anhui 243002, P. R. China

[7]These authors contributed equally to this work.

[*]Corresponding author. E-mail: gengzg@ustc.edu.cn (Z.G.); E-mail: zengj@ustc.edu.cn (J.Z.).

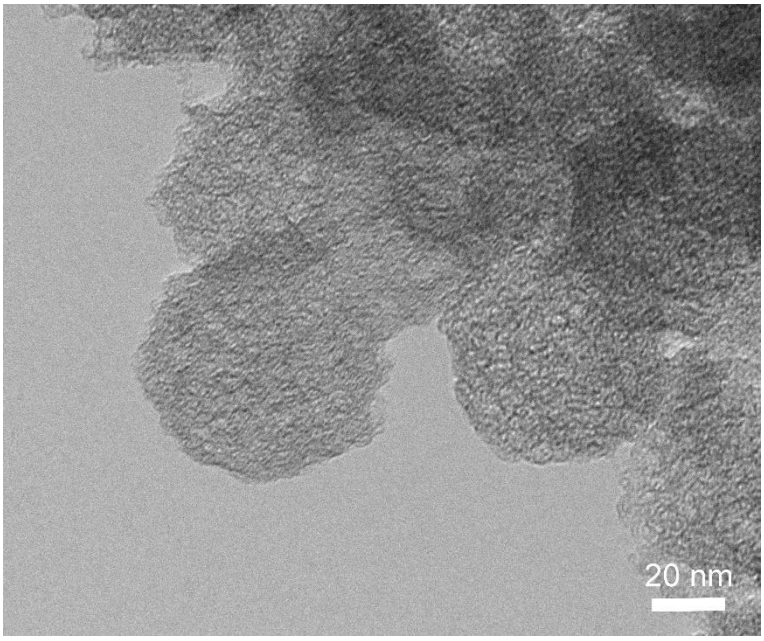


**Supplementary Fig. 1. TEM image of $Cu_1$-N-C**. $Cu_1$-N-C exhibited the amorphous carbon structure without any observable metallic particles.

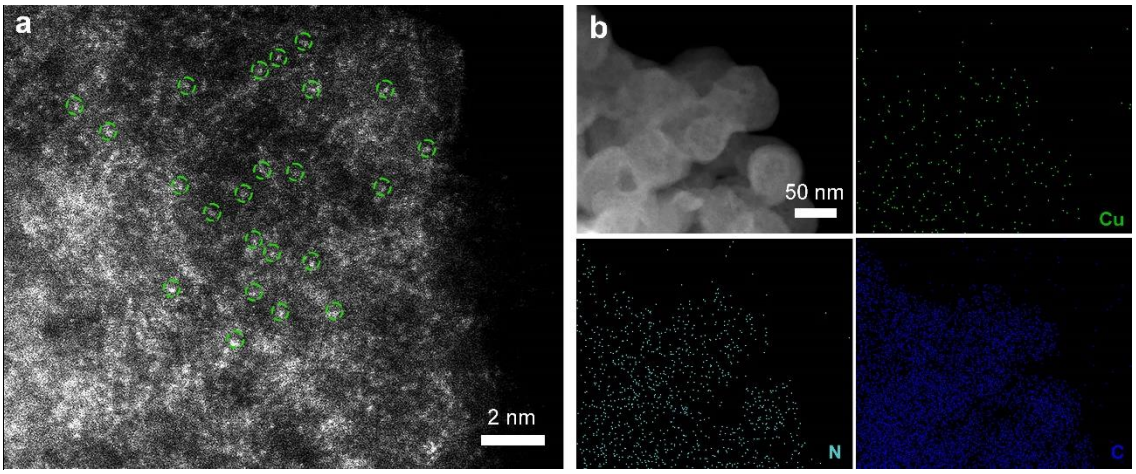


**Supplementary Fig. 2. Characterization of $Cu_1$-N-C.** (**a**) Aberration-corrected HAADF-STEM image and (**b**) EDS elemental mapping results of $Cu_1$-N-C. These results demonstrate the atomically dispersed Cu in $Cu_1$-N-C.

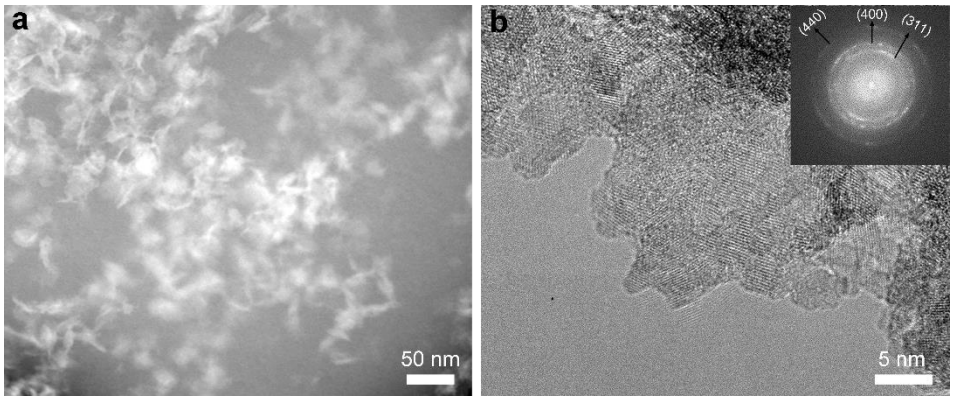


**Supplementary Fig. 3. Characterization of $Co_3O_4/Cu_1$-N-C.** (**a**) HAADF-STEM image of $Co_3O_4/Cu_1$-N-C and (**b**) HRTEM image and the corresponding SAED pattern (the inset) of $Co_3O_4/Cu_1$-N-C. The lattice fringe distances were well indexed to (311), (400), and (440) planes of $Co_3O_4$, confirming the successful formation of $Co_3O_4$.

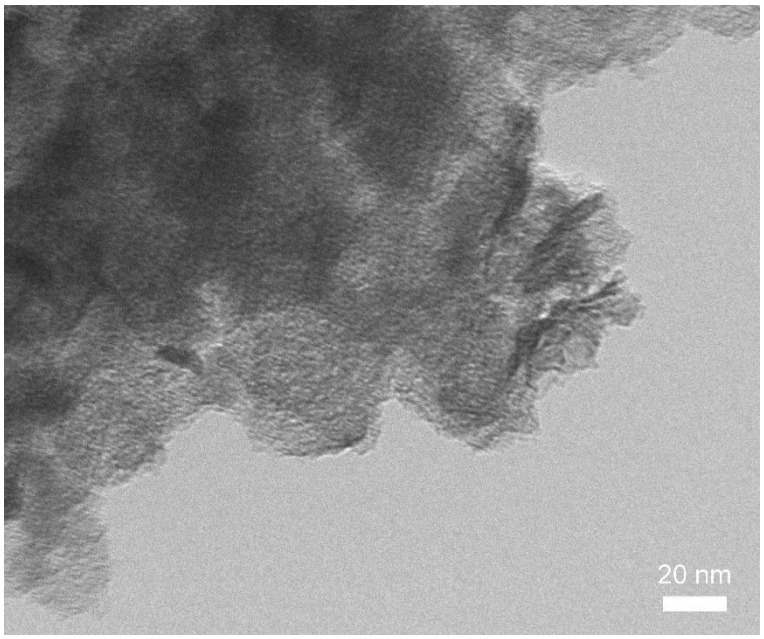


**Supplementary Fig. 4. TEM image of $Co_3O_4$/N-C.**

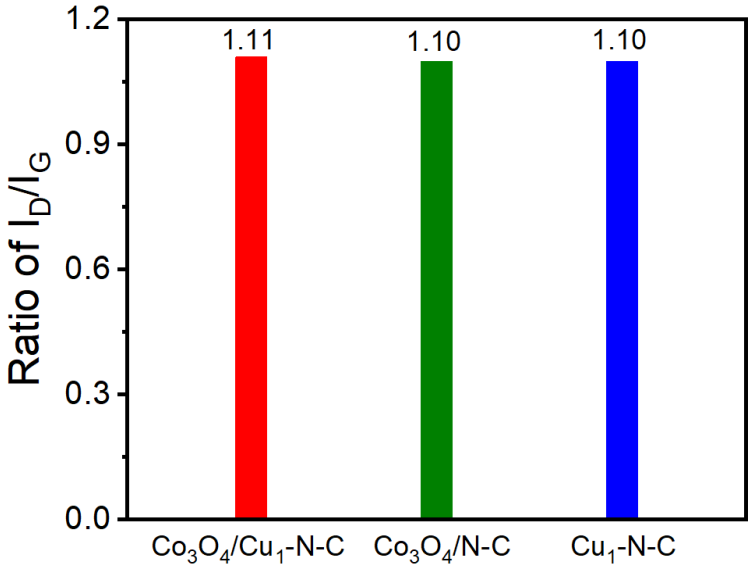


**Supplementary Fig. 5. The ratio of $I_D/I_G$ for $Co_3O_4/Cu_1$-N-C, $Co_3O_4$/N-C and $Cu_1$-N-C.**

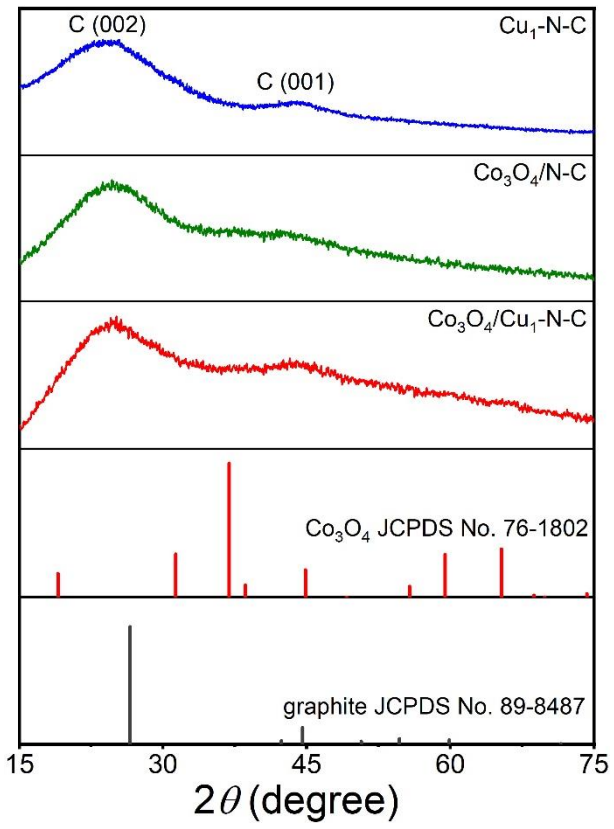


**Supplementary Fig. 6. XRD patterns of $Cu_1$-N-C, $Co_3O_4$/N-C, and $Co_3O_4/Cu_1$-N-C.** The three samples all exhibited two broad peaks at 24.5° and 44.0°, which were attributed to the (002) and (001) facets of graphite carbon.

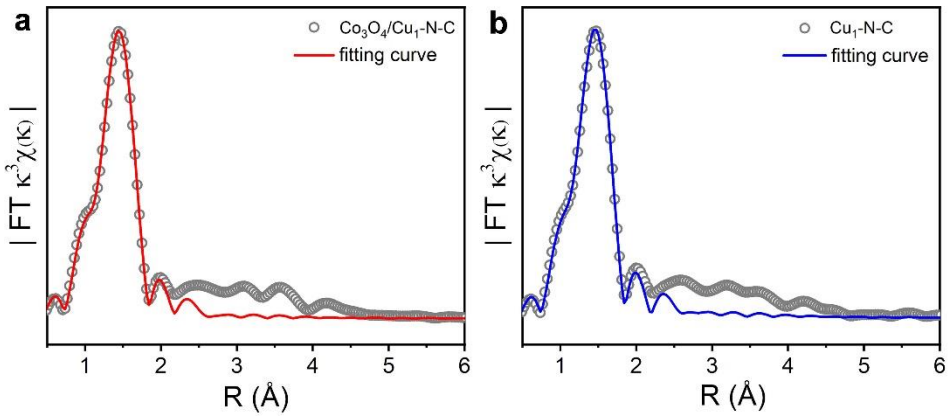


**Supplementary Fig. 7. Cu *K*-edge EXAFS fitting curves of (a) $Co_3O_4/Cu_1$-N-C and (b) $Cu_1$-N-C.**

**Supplementary Table 1. EXAFS data fitting results of $Co_3O_4/Cu_1$-N-C and $Cu_1$-N-C.**

| Sample | Shell | *CN* | R (Å) | $\sigma^2$ | $\Delta E_0$ (eV) |
|---|---|---|---|---|---|
| $Co_3O_4/Cu_1$-N-C | Cu-N | 3.7 ± 0.7 | 1.93 ± 0.03 | 0.007 | 1.3 |
| $Cu_1$-N-C | Cu-N | 3.9 ± 0.7 | 1.93 ± 0.03 | 0.007 | 0.4 |

*CN* represents coordination number, R represents bond distance, $\sigma^2$ represents Debye-Waller factor, and $\Delta E_0$ represents edge-energy shift.

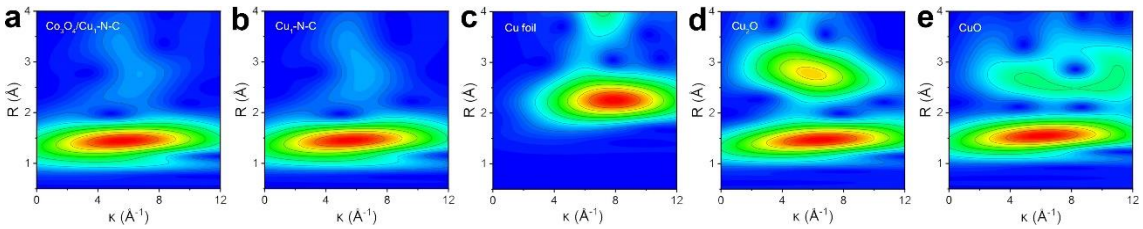


**Supplementary Fig. 8. Wavelet transformed EXAFS spectra of (a) $Co_3O_4$/$Cu_1$-N-C, (b) $Cu_1$-N-C, (c) Cu foil, (d) $Cu_2O$ and (e) CuO.** The WT-EXAFS spectra of $Co_3O_4$/$Cu_1$-N-C and $Cu_1$-N-C both showed the maximum intensity at around 5.6 $Å^{-1}$, demonstrating the Cu-N coordination structure in the two catalysts.

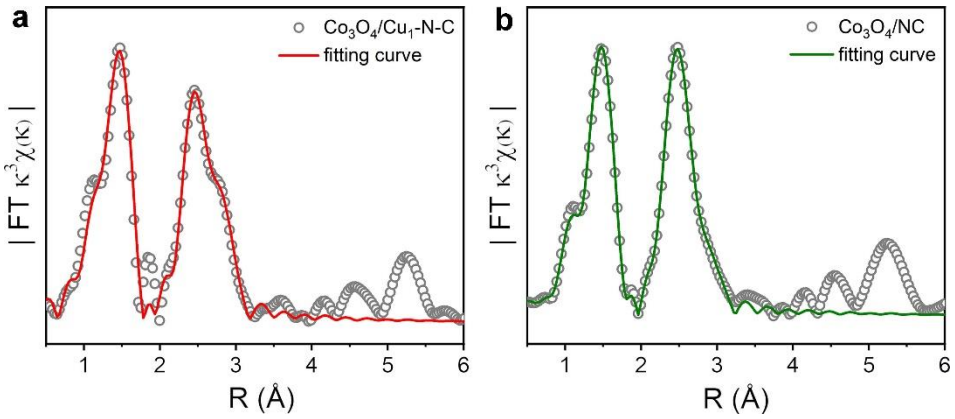


**Supplementary Fig. 9. Co *K*-edge EXAFS fitting curves of (a) $Co_3O_4/Cu_1$-N-C and (b) $Co_3O_4$/N-C.** The coordination structure of $Co_3O_4$ species were similar on the $Cu_1$-N-C and N-doped carbon supports.

**Supplementary Table 2. EXAFS data fitting results of Co *K*-edge for $Co_3O_4/Cu_1$-N-C and $Cu_1$-N-C.**

| Sample | Shell | *CN* | R (Å) | $\sigma^2$ | $\Delta E_0$ (eV) |
|---|---|---|---|---|---|
| $Co_3O_4/Cu_1$-N-C | Co-O | 4.0 ± 0.8 | 1.89 ± 0.03 | 0.007 | -4.7 |
| | Co-O-Co | 2.0 ± 0.4 | 2.86 ± 0.03 | 0.005 | -2.1 |
| | Co-O-Co | 1.9 ± 0.4 | 3.09 ± 0.03 | 0.008 | -2.1 |
| $Co_3O_4$/N-C | Co-O | 4.2 ± 0.8 | 1.89 ± 0.03 | 0.004 | -4.2 |
| | Co-O-Co | 2.6 ± 0.5 | 2.84 ± 0.03 | 0.005 | 1.2 |
| | Co-O-Co | 0.6 ± 0.1 | 3.16 ± 0.03 | 0.005 | 1.2 |

*CN* represents coordination number, R represents bond distance, $\sigma^2$ represents Debye-Waller factor, and $\Delta E_0$ represents edge-energy shift.

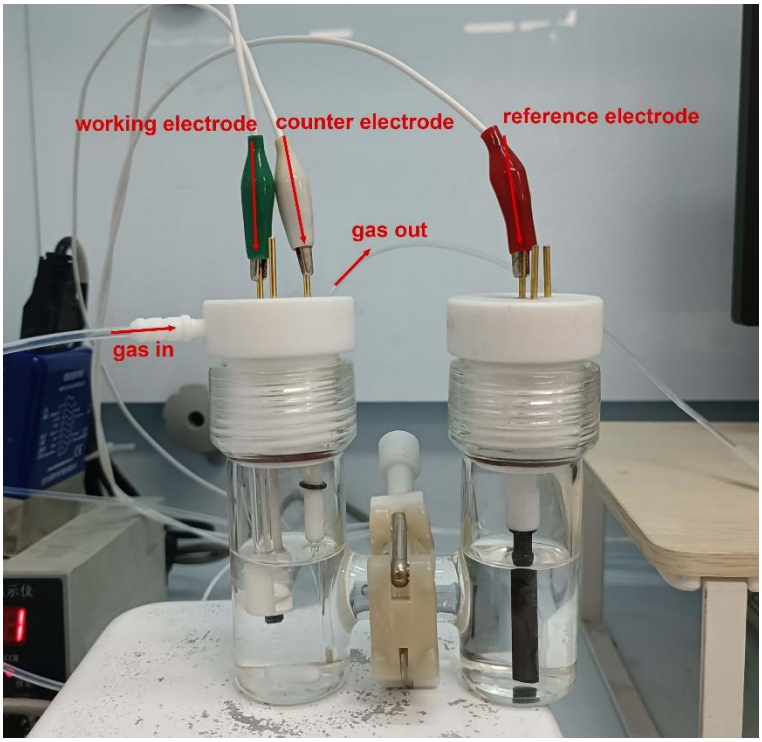


**Supplementary Fig. 10. The photograph of the H-cell during the electrochemical measurements.**

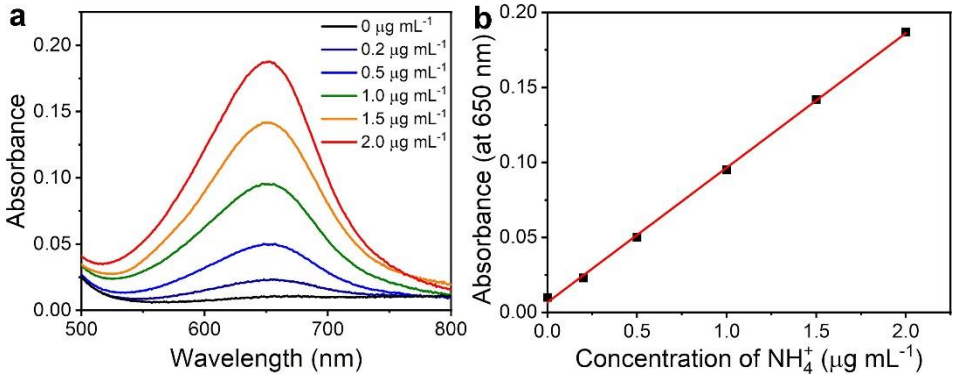


**Supplementary Fig. 11. Determination of $NH_4^+$.** (**a**) UV-vis curves and (**b**) concentration-absorbance curve of $NH_4^+$ solution with a series of standard concentrations. The standard curve showed linear relation of absorbance with $NH_4^+$ concentration ($y = 0.089x + 0.006$, $R^2 = 0.9992$).

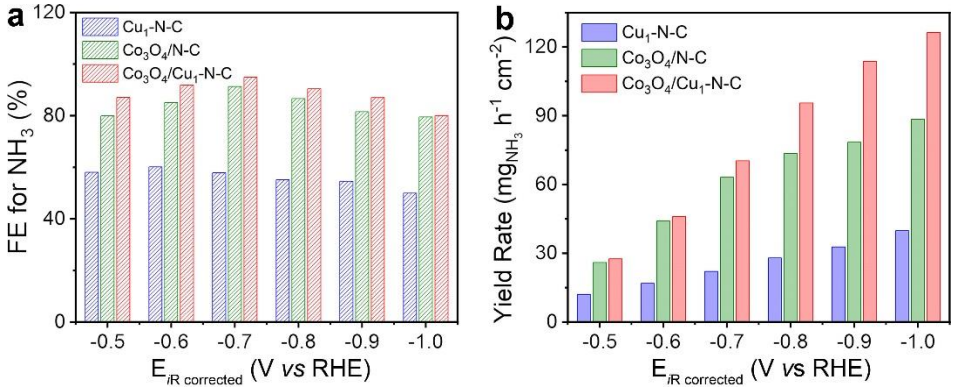


**Supplementary Fig. 12. Catalytic performance toward $NO_2^-$ electroreduction.** (**a**) FE for $NH_3$ and (**b**) yield rate for $NH_3$ of $Cu_1$-N-C, $Co_3O_4$/N-C, and $Co_3O_4/Cu_1$-N-C at different applied potentials in 1 M $NO_2^-$.

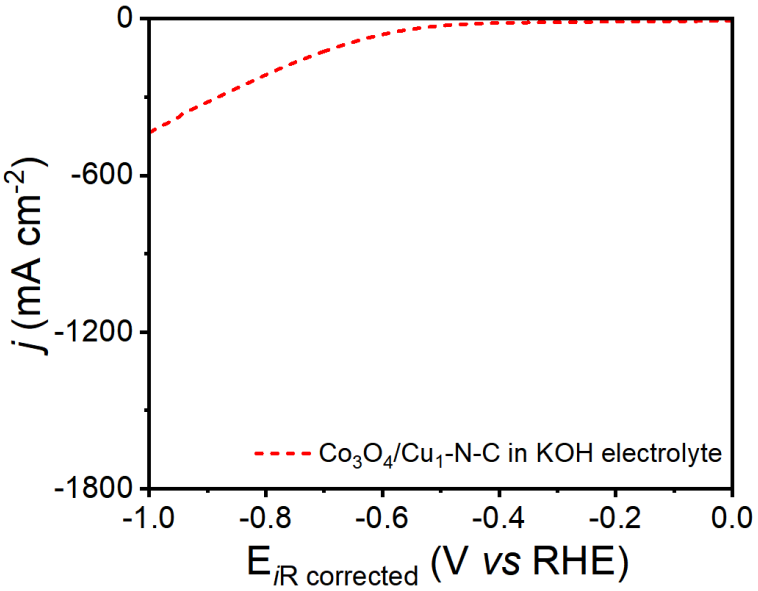


**Supplementary Fig. 13. LSV curve of $Co_3O_4/Cu_1$-N-C in 1 M KOH electrolyte without $NO_3^-$.**

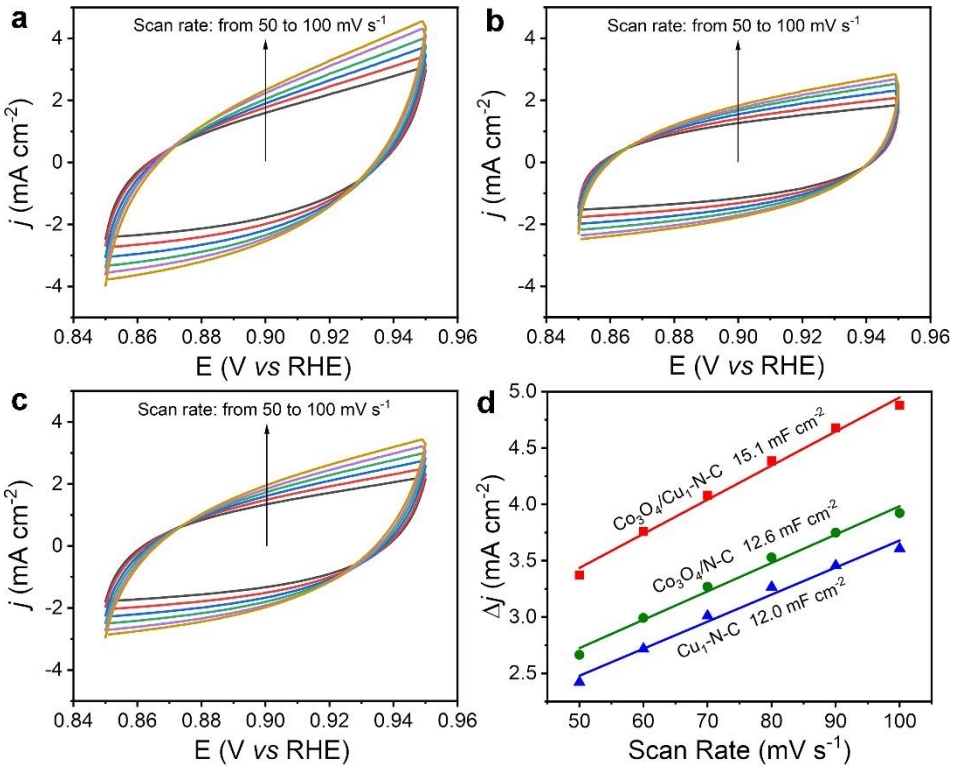


**Supplementary Fig. 14. CV curves and charging current density differences of $Co_3O_4$/$Cu_1$-N-C, $Cu_1$-N-C, and $Co_3O_4$/N-C.** CV curves for (**a**) $Co_3O_4$/$Cu_1$-N-C, (**b**) $Cu_1$-N-C, and (**c**) $Co_3O_4$/N-C at different scan rates from 50 to 100 mV $s^{-1}$, respectively. (**d**) Charging current density differences plotted against scan rates of $Co_3O_4$/$Cu_1$-N-C, $Cu_1$-N-C, and $Co_3O_4$/N-C.

**Supplementary Table 3. The comparison of catalytic performance over recently reported electrocatalysts toward $NO_3^-$ electroreduction.**

| Catalysts | Mass loading (mg $cm^{-2}$) | Potential (V vs RHE) | Electrolyte | Stability | Electrode type | FE (%) | Yield rate ($mg_{NH_3}$ $h^{-1}$ $cm^{-2}$) | Ref. |
|---|---|---|---|---|---|---|---|---|
| $Cu_{50}Ni_{50}$ | / | -0.15 | 0.1 M $NO_3^-$ + 0.1 M KOH | 12 h | Glassy carbon | 99.0 | / | [1] |
| CuCoSP | / | -0.175 | 0.1 M $NO_3^-$ + 0.1 M KOH | 10 h | Cu foil | ~90.6 | 19.9 | [2] |
| Rh@Cu-0.6% | / | -0.2 | 0.1 M $NO_3^-$ + 0.05 M $Na_2SO_4$ | 14 h | Cu foil | 93.0 | 21.6 | [3] |
| Cu-N-C SAC | 1.33 | -1.0 | 0.1 M $NO_3^-$ + 0.1 M KOH | 20 cycles | Carbon paper | 84.7 | 4.5 | [4] |
| $CoO_x$ | 1.75 | -0.3 | 0.1 M $NO_3^-$ + 0.1 M KOH | / | Carbon cloth | 93.4 | 2.9 | [5] |
| Ru-CuNW | / | -0.135 | 0.1 M $NO_3^-$ + 1 M KOH | / | Cu foam | 95.6 | 76.5 | [6] |
| $Ni_{35}$/NC-sd | 2 | -0.5 | 0.3 M $NO_3^-$ + 0.5 M $Na_2SO_4$ | 5 cycles | Ti mesh | 99 | 5.1 | [7] |
| Ti foil | / | -1.0 | 0.3 M $NO_3^-$ + 0.1 M $HNO_3$ | 8 h | Ti foil | 82 | / | [8] |
| MWCNTs | 0.4 | -0.85 | 0.4 M $NO_3^-$ + 0.1 M PBS | / | Carbon paper | 73 | / | [9] |
| Fe SAC | 0.4 | -0.85 | 0.5 M $NO_3^-$ + 0.1 M $Na_2SO_4$ | 20 cycles | Glassy carbon | 74.9 | 7.8 | [10] |
| CoP NAs/CFC | 0.1143 | -0.5 | 1 M $NO_3^-$ + 1 M NaOH | 20 h | Glassy carbon | ~100 | 16.3 | [11] |
| Ru-ST-12 | 0.185 | -1.0 | 1 M $NO_3^-$ + 1 M KOH | 100 h | Carbon paper | ~100 | 19.9 | [12] |
| CNS-CoP | / | -1.03 | 1 M $NO_3^-$ + 1 M KOH | 123 h | Carbon cloth | 90.5 | 55.7 | [13] |
| Ir nanotubes | / | 0.06 | 1 M $NO_3^-$ + 0.1 M $HClO_4$ | / | Glassy carbon | 84.7 | / | [14] |

| | | | | | | | | |
|---|---|---|---|---|---|---|---|---|
| Bi-Clred | 0.51 | -0.8 | 1 M $NO_3^-$ + 1 M KOH | 6 cycles | Glassy carbon | ~75 | ~28 | [15] |
| Cu/CuAu | 0.2 | -0.6 | 1 M $NO_3^-$ + 1 M KOH | 20 cycles | Carbon paper | 85.5 | 1.7 | [16] |
| $Co_3O_4$/Cu NC | 1 | -1.0 | 1 M $NO_3^-$ + 1 M KOH | 20 cycles | Carbon paper | 97.7 | 114.0 | This work |

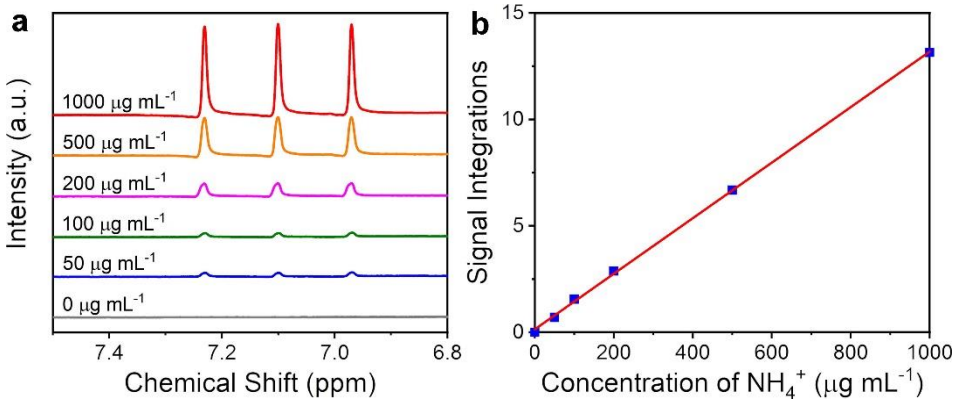


**Supplementary Fig. 15. Determination of $NH_4^+$.** (**a**) $^1H$ NMR spectra of standard $(NH_4)_2SO_4$ solutions with a series of standard concentrations, respectively. (**b**) Concentration-integral area curve for the standard $(NH_4)_2SO_4$ solutions. The standard curve showed linear relation of signal integration with $NH_4^+$ ion concentration ($y = 0.013x + 0.137$, $R^2 = 0.9994$).

**Supplementary Table 4. The yield rate of $NH_3$ ($mg_{NH3}$ $h^{-1}$ $cm^{-2}$) over $Co_3O_4/Cu_1$-N-C determined by indophenol blue method and $^1H$ NMR method, respectively.**

| The applied potential | Indophenol blue method | $^1H$ NMR |
|---|---|---|
| -0.5 V *vs* RHE | 36.7 | 37.0 |
| -0.6 V *vs* RHE | 50.9 | 49.9 |
| -0.7 V *vs* RHE | 65.7 | 66.4 |
| -0.8 V *vs* RHE | 91.7 | 89.6 |
| -0.9 V *vs* RHE | 109.4 | 106.9 |
| -1.0 V *vs* RHE | 114.0 | 112.7 |

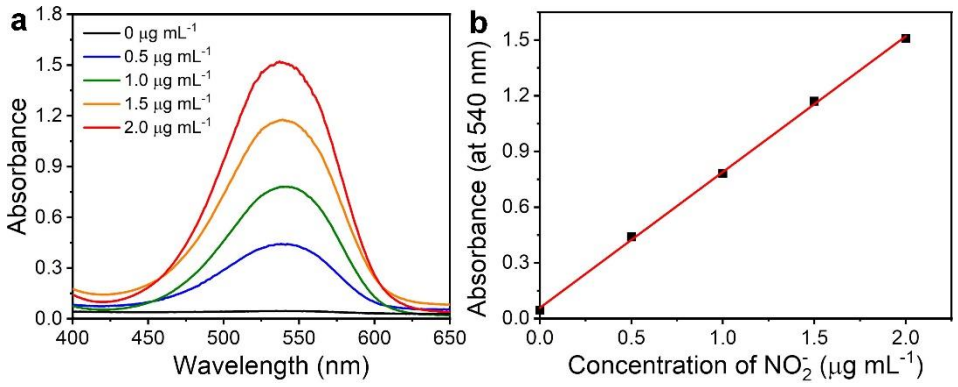


**Supplementary Fig. 16. Determination of $NO_2^-$.** (**a**) UV-vis curves and (**b**) concentration-absorbance curve of $NO_2^-$ solution with a series of standard concentrations. The standard curve showed linear relation of absorbance with $NO_2^-$ concentration ($y = 0.731x + 0.058$, $R^2 = 0.9991$).

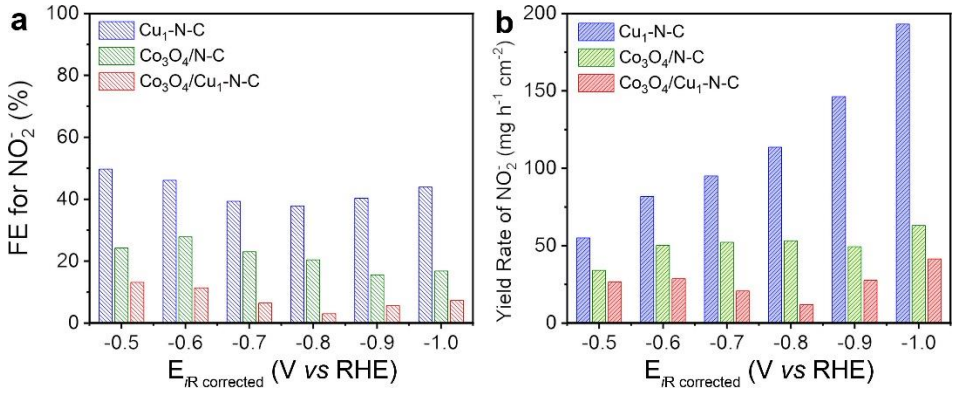


**Supplementary Fig. 17. Catalytic performance for $NO_2^-$ production.** (**a**) FE for $NO_2^-$ and (**b**) yield rate of $NO_2^-$ over $Cu_1$-N-C, $Co_3O_4$/N-C, and $Co_3O_4/Cu_1$-N-C at different applied potentials in 1 M $NO_3^-$, respectively. Among the three catalysts, $Cu_1$-N-C exhibited the highest FE for $NO_2^-$, indicating the excessive accumulation of $NO_2^-$ during the electroreduction of $NO_3^-$, which hampered the formation of $NH_3$ for $Cu_1$-N-C. Notably, FE for $NO_2^-$ of $Co_3O_4/Cu_1$-N-C was much lower than that of $Cu_1$-N-C, suggesting that the composition of $Co_3O_4$ with $Cu_1$-N-C promoted the subsequent conversion of $NO_2^-$.

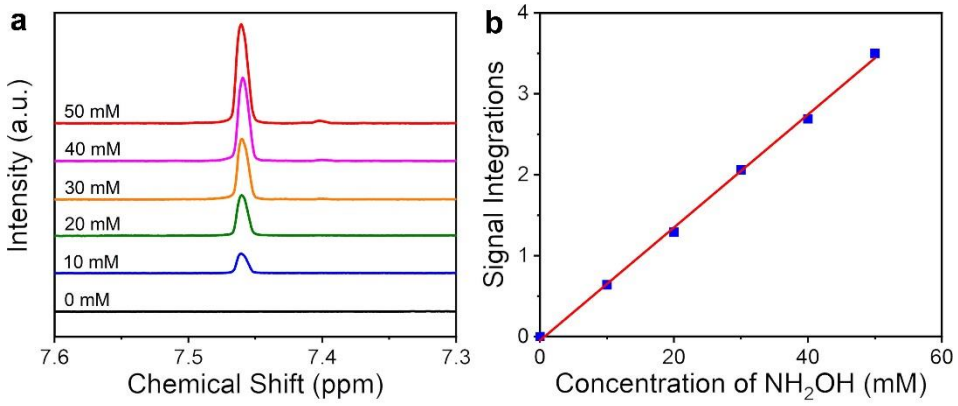


**Supplementary Fig. 18. Determination of $NH_2OH$.** (**a**) $^1H$ NMR spectra of standard $NH_2OH$ solutions with a series of standard concentrations, respectively. (**b**) Concentration-integral area curve for the standard $NH_2OH$ solutions. The standard curve showed linear relation of signal integration with $NH_2OH$ concentration ($y = 0.070x - 0.048$, $R^2 = 0.9982$).

**Supplementary Table 5. The FE of other products over $Co_3O_4/Cu_1$-N-C toward $NO_3^-$ and $NO_2^-$ electroreduction at -0.8 V *vs* RHE, respectively.**

| | $NO_3^-$ electroreduction | $NO_2^-$ electroreduction |
|---|---|---|
| $NH_3$ | 97.7% | 94.9% |
| $NH_2OH$ | / | / |
| NO | 0.6% | 1.3% |
| $NO_2$ | / | / |
| $N_2O$ | 0.5% | 0.8% |
| $N_2$ | 2.0% | 7.3% |
| $H_2$ | 0.6% | 0.3% |

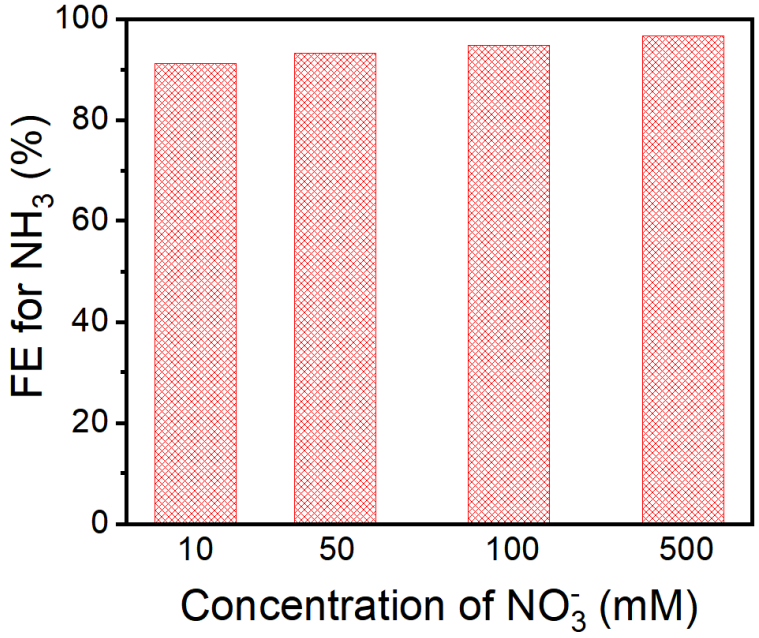


**Supplementary Fig. 19. The FE for $NH_3$ over $Co_3O_4$/$Cu_1$-N-C at different concentrations of $NO_3^-$ ranging from 10 mM to 500 mM.**

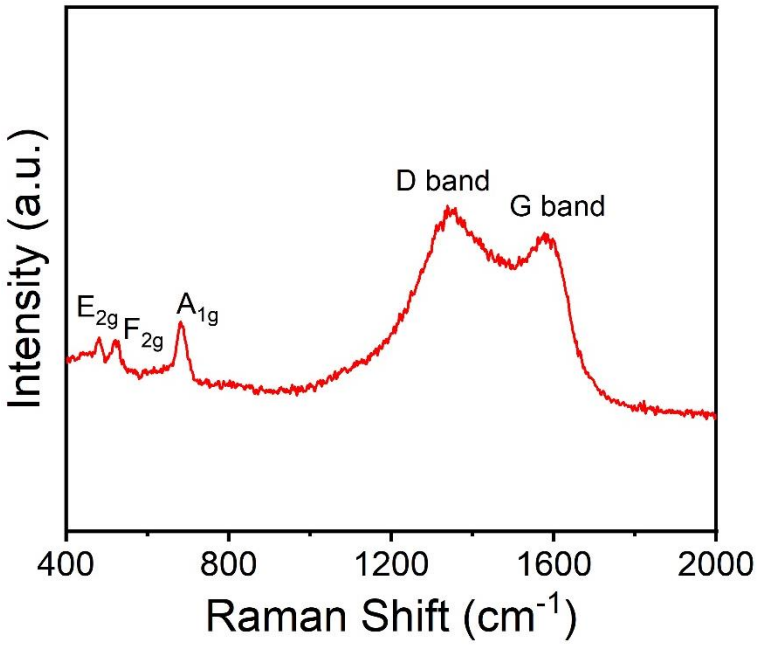


**Supplementary Fig. 20. Raman spectrum for $Co_3O_4/Cu_1$-N-C after the electrolysis.**

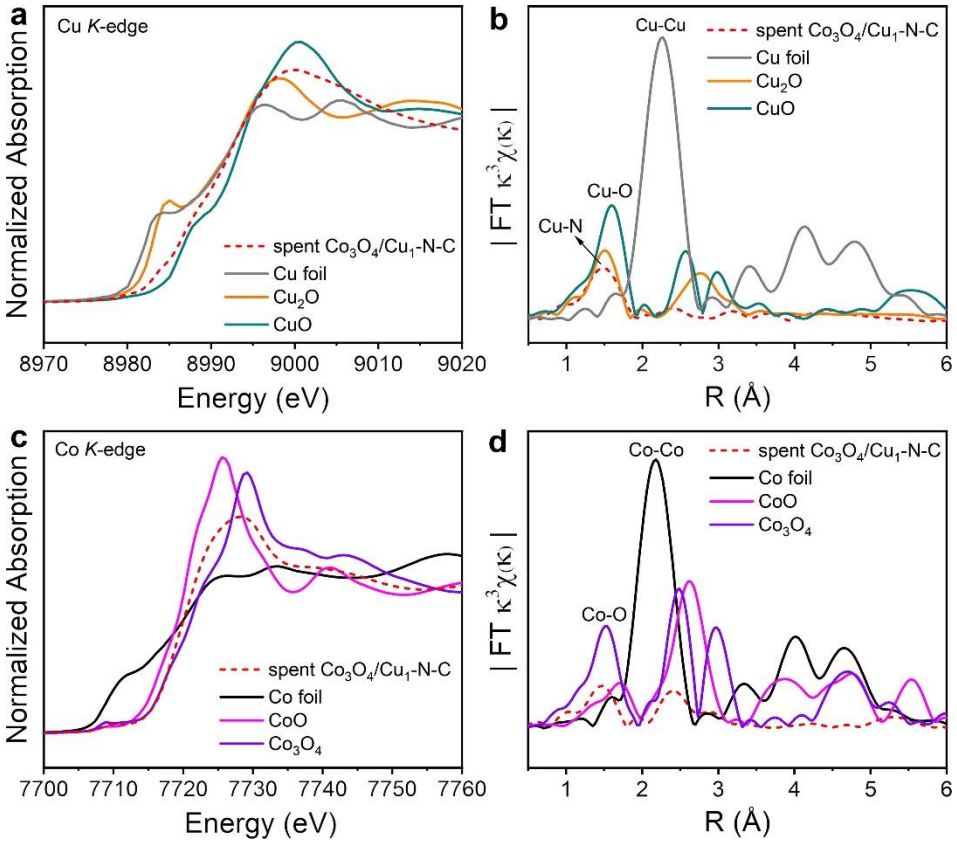


**Supplementary Fig. 21. Characterization of $Co_3O_4/Cu_1$-N-C after the electrolysis.** Cu *K*-edge (**a**) XANES spectra and (**b**) EXAFS spectra for $Co_3O_4/Cu_1$-N-C after the electrolysis, Cu foil, $Cu_2O$, and CuO. Co *K*-edge (**c**) XANES spectra and (**d**) EXAFS spectra for $Co_3O_4/Cu_1$-N-C after the electrolysis, Co foil, CoO, and $Co_3O_4$.

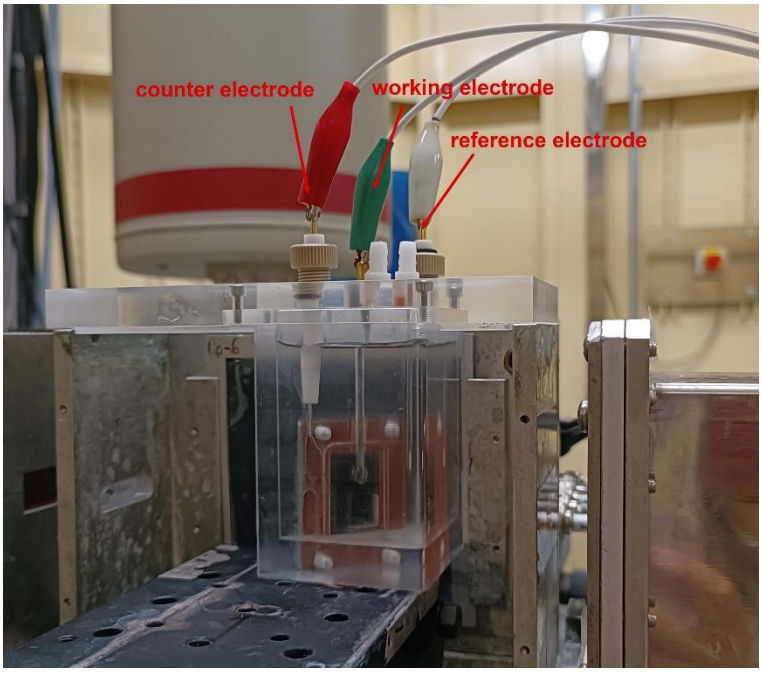


**Supplementary Fig. 22. A photograph of the homemade in situ XAFS cell during the operation.**

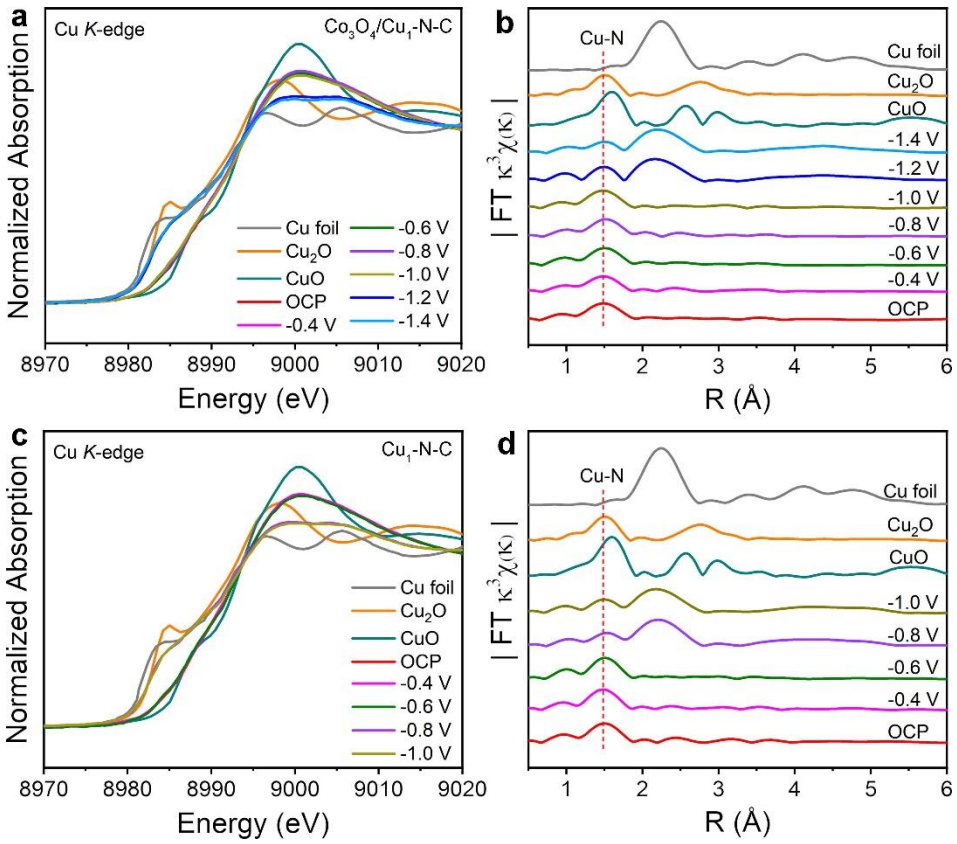


**Supplementary Fig. 23. *In situ* Cu *K*-edge (a) XANES spectra and (b) EXAFS spectra for $Co_3O_4/Cu_1$-N-C. *In situ* Cu *K*-edge (c) XANES spectra and (d) EXAFS spectra for $Cu_1$-N-C.** As the potentials increased from -0.4 V to -1.0 V *vs* RHE, the edge profiles of *in situ* XANES spectra for $Co_3O_4/Cu_1$-N-C showed no discernible change (Supplementary Fig. 23a). Moreover, no Cu-Cu bond was observed in the EXAFS spectra, demonstrating that Cu single atoms remained in the atomically dispersed state under the potentials of electrochemical tests (Supplementary Fig. 23b). However, when the potentials further increased, a prominent decline in the edge energy of XANES spectra was observed and the peak of Cu-Cu bond appeared in the EXAFS spectra for $Co_3O_4/Cu_1$-N-C. These phenomena manifested that the Cu atoms aggregated into clusters under the potential as high as -1.2 V *vs* RHE. With regard to $Cu_1$-N-C, the decrease in the edge energy of XANES spectra and the emergence of Cu-Cu bond were both discerned at -0.8 V *vs* RHE (Supplementary Figs. 23c and d). The introduction of $Co_3O_4$ nanosheets partly prevented the aggregation of Cu atoms, which might be attributed to the segregation of Cu atoms in $Cu_1$-N-C by $Co_3O_4$ nanosheets as the fence, requiring higher energy to drive the separated Cu atom in $Co_3O_4/Cu_1$-N-C to aggregate into particles.

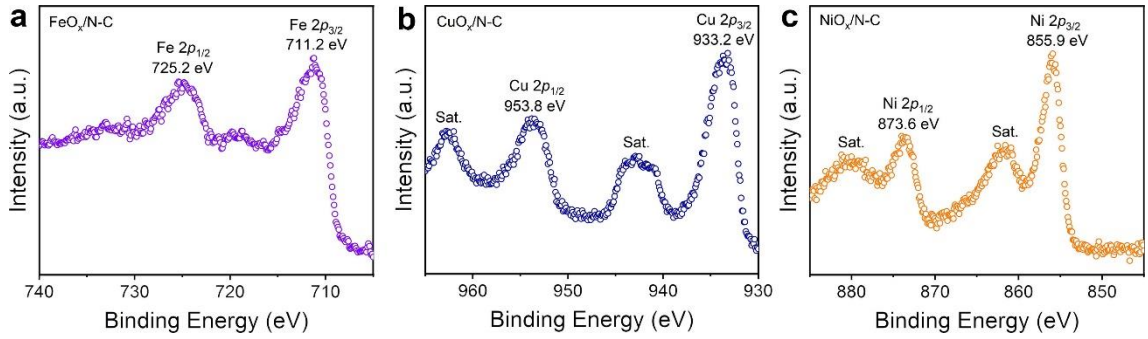


**Supplementary Fig. 24. (a) Fe 2*p* XPS spectra of $FeO_x$/N-C, (b) Cu 2*p* XPS spectra of $CuO_x$/N-C, and (c) Ni 2*p* XPS spectra of $NiO_x$/N-C.** The Fe 2*p* XPS spectra of $FeO_x$/N-C exhibited two signals at 725.2 and 711.2 eV, which were attributed to $Fe^{3+}$ $2p_{1/2}$ and $Fe^{3+}$ $2p_{3/2}$, respectively. The Cu 2*p* XPS spectra of $CuO_x$/N-C showed two peaks at 953.8 and 933.2 eV, which were assigned to $Cu^{2+}$ $2p_{1/2}$ and $Cu^{2+}$ $2p_{3/2}$, respectively. The Ni 2*p* XPS spectra of $NiO_x$/N-C displayed two signals at 837.6 and 855.9 eV, which were assigned to $Ni^{2+}$ $2p_{1/2}$ and $Ni^{2+}$ $2p_{3/2}$, respectively.

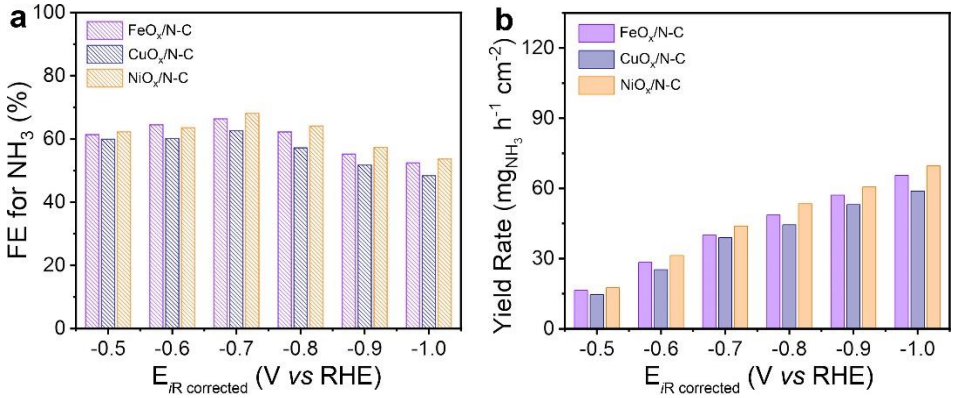


**Supplementary Fig. 25. Catalytic performance of $FeO_x$/N-C, $CuO_x$/N-C, and $NiO_x$/N-C.** (**a**) FE for $NH_3$ and (**b**) yield rate for $NH_3$ of $FeO_x$/N-C, $CuO_x$/N-C, and $NiO_x$/N-C at different applied potentials with 1 M $NO_2^-$.

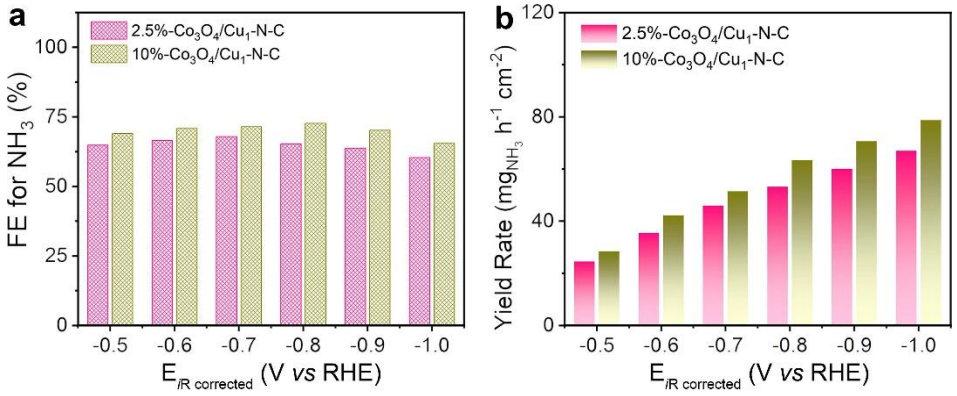


**Supplementary Fig. 26. Catalytic performance of $Co_3O_4/Cu_1$-N-C with different loading of $Co_3O_4$.** (**a**) FE for $NH_3$ and (**b**) yield rate of $NH_3$ over $Co_3O_4/Cu_1$-N-C prepared by controlling the amount of Co precursor as 22.5 and 67.5 mg, respectively. The corresponding samples were denoted as 2.5%-$Co_3O_4/Cu_1$-N-C and 10%-$Co_3O_4/Cu_1$-N-C, respectively. The insufficient loading of $Co_3O_4$ on $Cu_1$-N-C could not ensure the efficient conversion of the accumulated $NO_2^-$, leading to undesirable performance. However, the excess amount of $Co_3O_4$ would completely cover the surface of $Cu_1$-N-C, impeding the fully exposure of Cu sites to adsorb $NO_3^-$. As such, the moderate ratio between Cu single atom and $Co_3O_4$ are beneficial to the performance of $NO_3^-$ electroreduction.

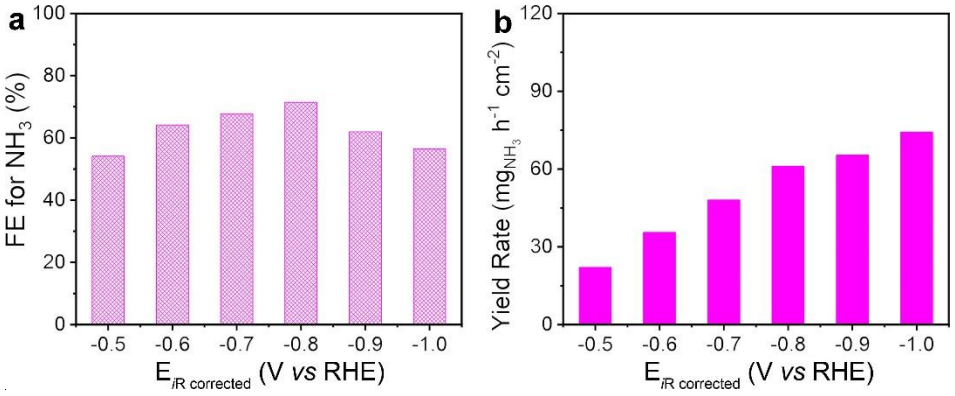


**Supplementary Fig. 27. Catalytic performance of physical mixing of $Cu_1$-N-C and $Co_3O_4$/N-C.** (**a**) FE for $NH_3$ and (**b**) yield rate of $NH_3$ over physical mixing of $Cu_1$-N-C and $Co_3O_4$/N-C at different applied potentials with 1 M $NO_3^-$.

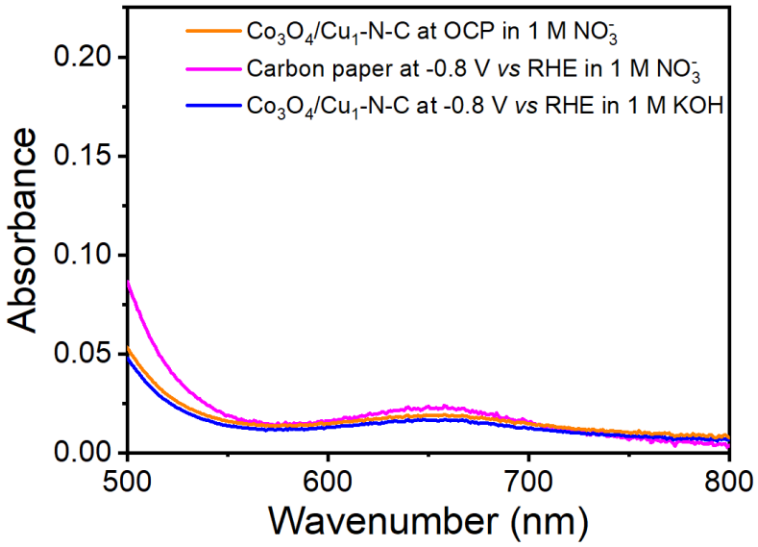


**Supplementary Fig. 28. UV-vis absorption spectra of the electrolyte under different conditions.**

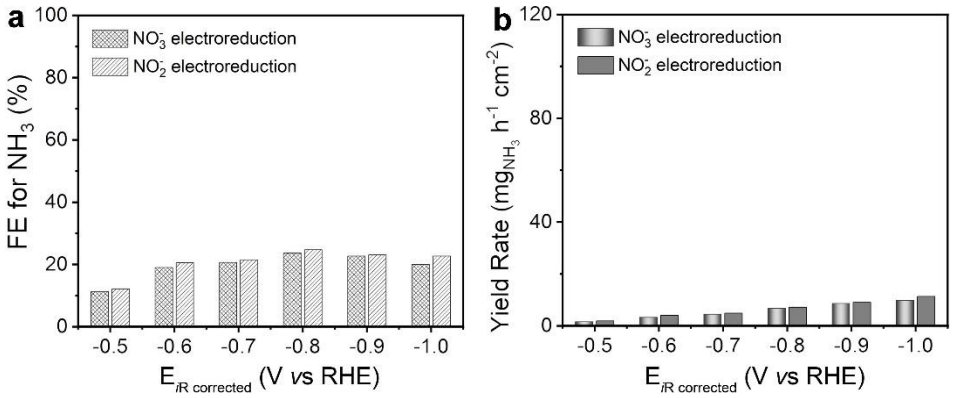


**Supplementary Fig. 29. Catalytic performance of N-doped carbon.** (**a**) FE for $NH_3$ and (**b**) yield rate for $NH_3$ of N-doped carbon at different applied potentials with 1 M $NO_3^-$/$NO_2^-$, respectively.

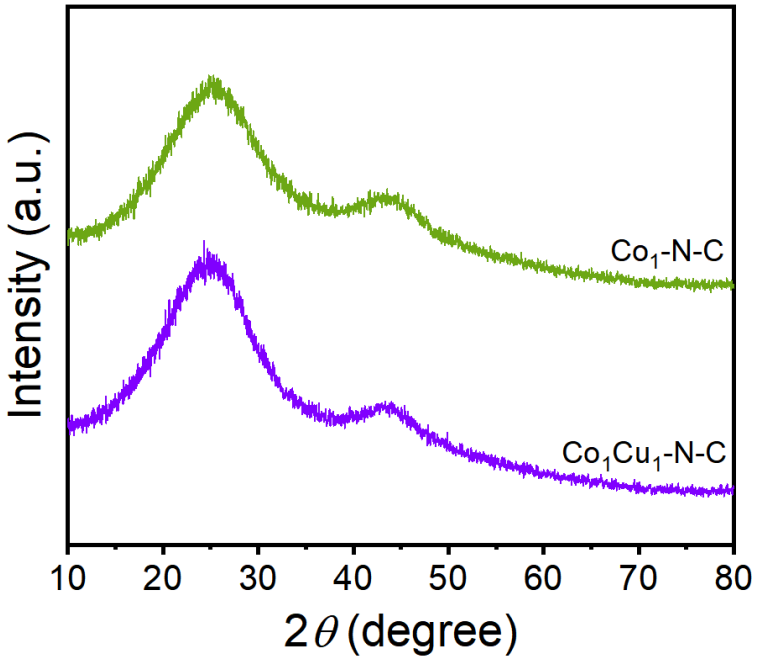


**Supplementary Fig. 30. XRD patterns of $Co_1$-N-C and $Co_1Cu_1$-N-C.** The XRD patterns of $Co_1$-N-C and $Co_1Cu_1$-N-C both exhibited the broad peaks which were attributed to graphite carbon. The characteristic peak of metal or metal oxides were not observed, demonstrating the absence of metal or metal oxides in the two samples.

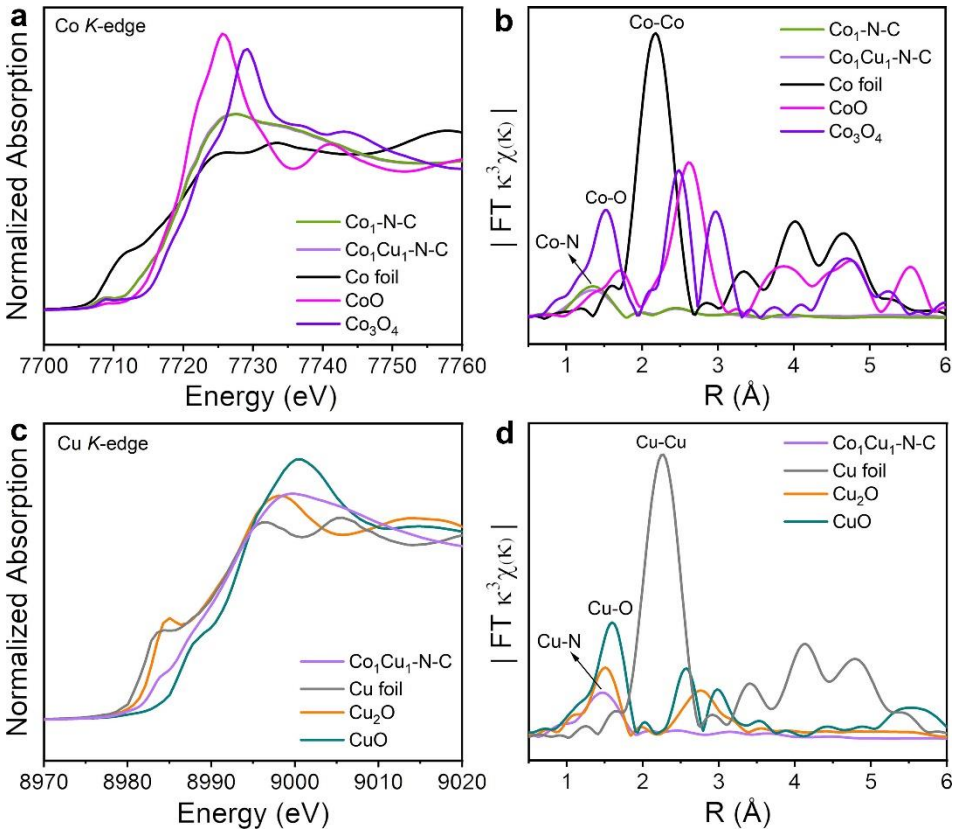


**Supplementary Fig. 31. XAFS results of $Co_1$-N-C and $Co_1Cu_1$-N-C.** Co *K*-edge (**a**) XANES spectra and (b) EXAFS spectra for $Co_1$-N-C, $Co_1Cu_1$-N-C, Co foil, CoO, and $Co_3O_4$. Cu *K*-edge (**c**) XANES spectra and (**d**) EXAFS spectra for $Co_1Cu_1$-N-C, Cu foil, $Cu_2O$, and CuO. The Co *K*-edge XANES spectra of $Co_1$-N-C and $Co_1Cu_1$-N-C both exhibited that the valence state of Co species were between +2 to +3. The absence of Co-Co bond in $Co_1$-N-C and $Co_1Cu_1$-N-C further confirmed the atomic dispersion of Co species. Besides, the absence of Cu-Cu bond in the Cu *K*-edge EXAFS spectra of $Co_1Cu_1$-N-C confirmed the atomic dispersion of Cu species in $Co_1Cu_1$-N-C. These results indicate that $Co_1$-N-C and $Co_1Cu_1$-N-C catalysts have been successfully prepared.

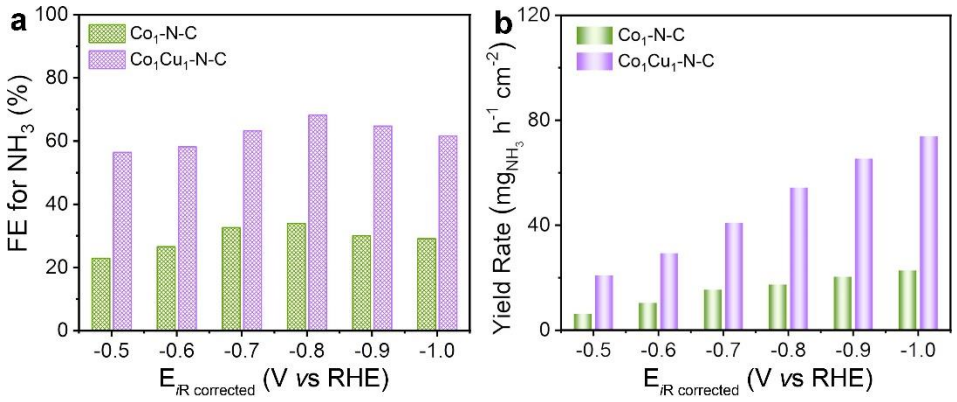


**Supplementary Fig. 32. Catalytic performance of $Co_1$-N-C and $Co_1Cu_1$-N-C.** (**a**) FE for $NH_3$ and (**b**) yield rate for $NH_3$ of $Co_1$-N-C and $Co_1Cu_1$-N-C at different applied potentials with 1 M $NO_3^-$. The interior catalytic performance over $Co_1Cu_1$-N-C than $Co_3O_4/Cu_1$-N-C suggests that synergetic role of Co single atoms and Cu single atoms were quite weak.

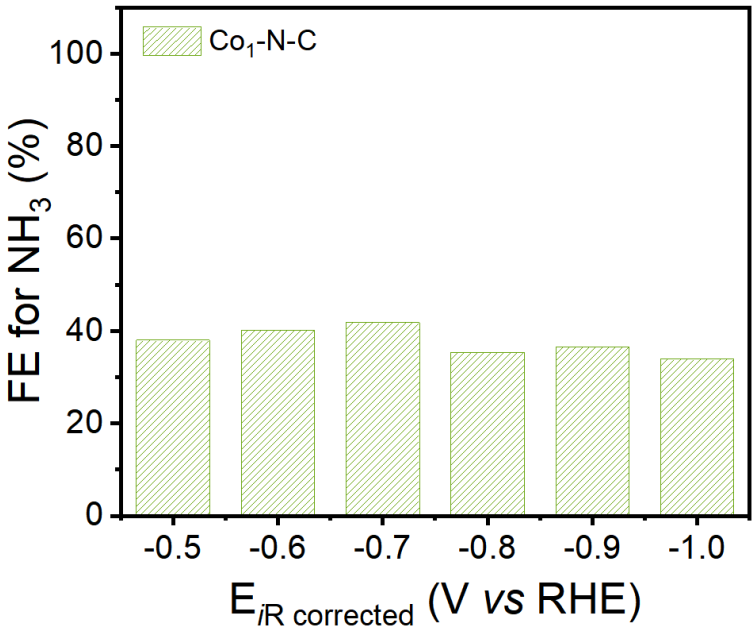


**Supplementary Fig. 33. FE for $NH_3$ of $Co_1$-N-C at different applied potentials with 1 M $NO_2^-$.** The FE for $NH_3$ of $Co_1$-N-C toward $NO_2^-$ electroreduction was much lower than that of $Co_3O_4$/N-C, indicating the sluggish conversion of $NO_2^-$ over Co single atoms.

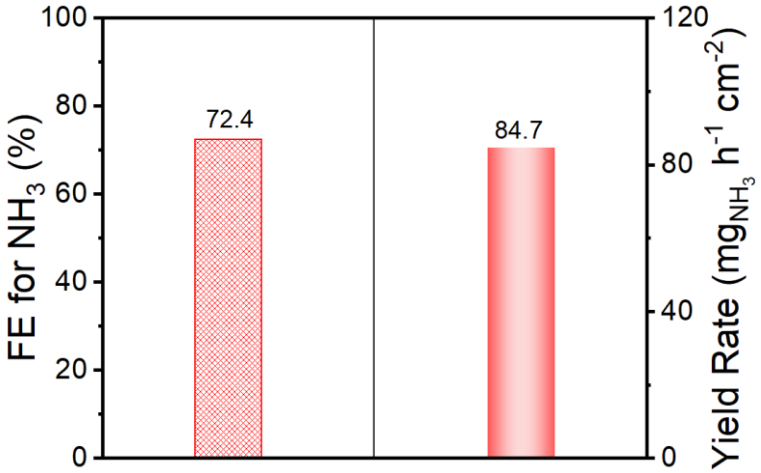


**Supplementary Fig. 34. The FE and yield rate for $NH_3$ of $Co_3O_4/Cu_1$-N-C without the magnetic stirring at -1.0 V *vs* RHE.**

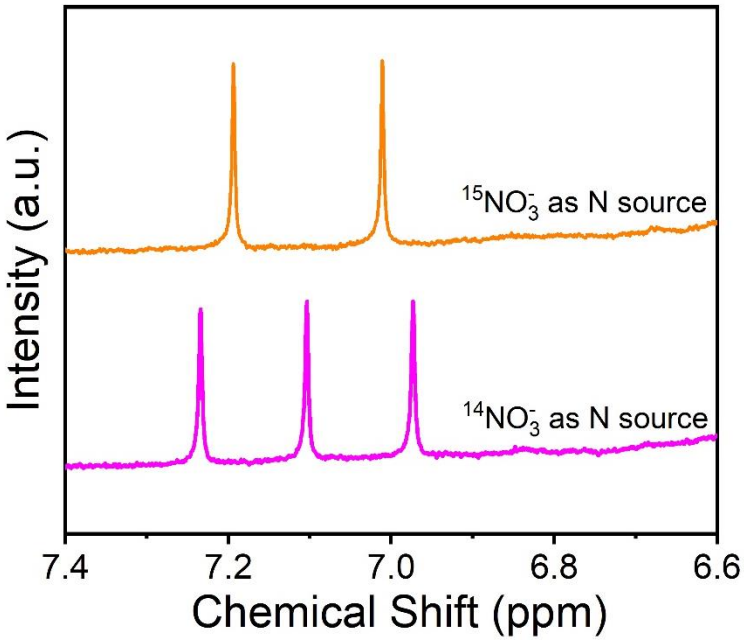


**Supplementary Fig. 35. $^{1}$H NMR spectra of the electrolyte after electroreduction reaction over $Co_3O_4/Cu_1$-N-C using $^{15}NO_3^-$ and $^{14}NO_3^-$ as the nitrogen source.**

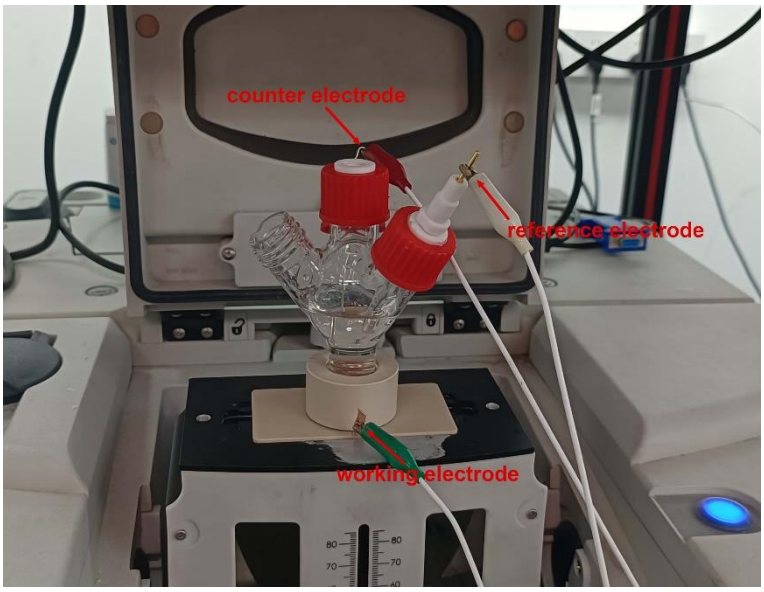


**Supplementary Fig. 36. A photograph of the homemade in situ FTIR cell during the operation.**

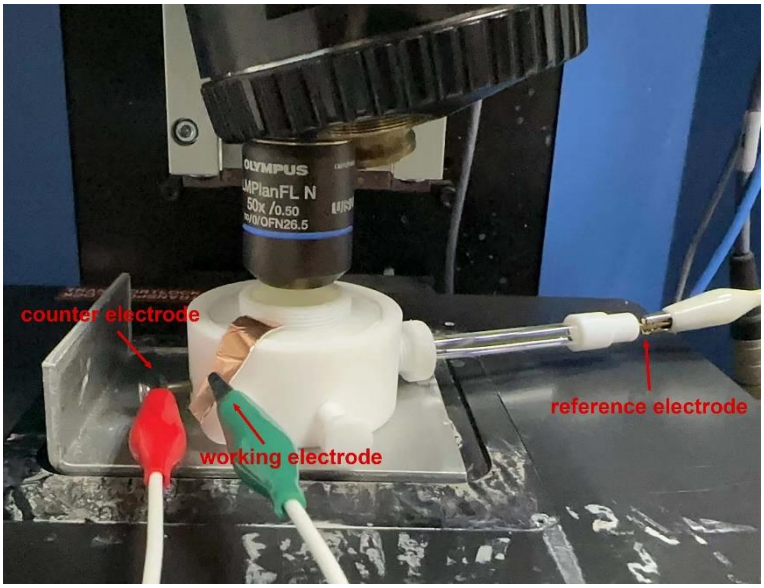


**Supplementary Fig. 37. A photograph of the homemade in situ Raman cell during the operation.**

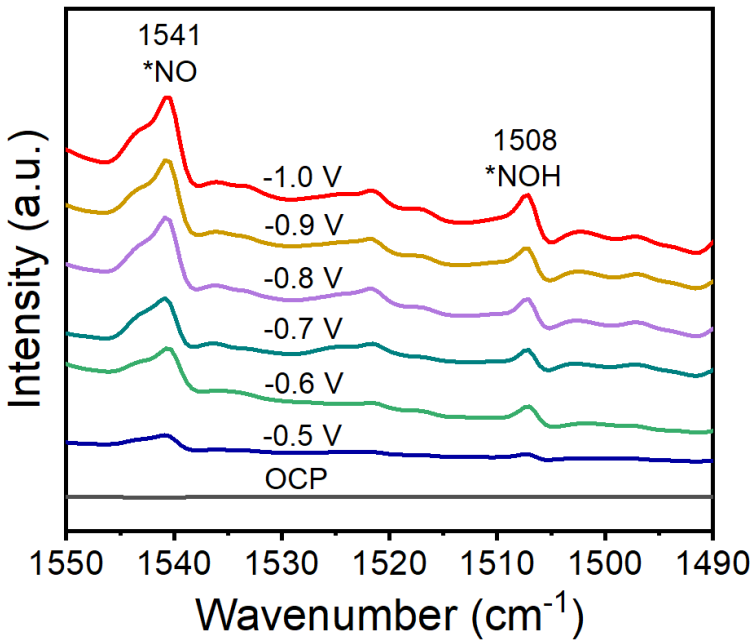


**Supplementary Fig. 38.** ***In situ*** **FTIR spectra for $Co_3O_4$/$Cu_1$-N-C from OCP to -1.0 V** ***vs*** **RHE in 1 M $NO_3^-$.**

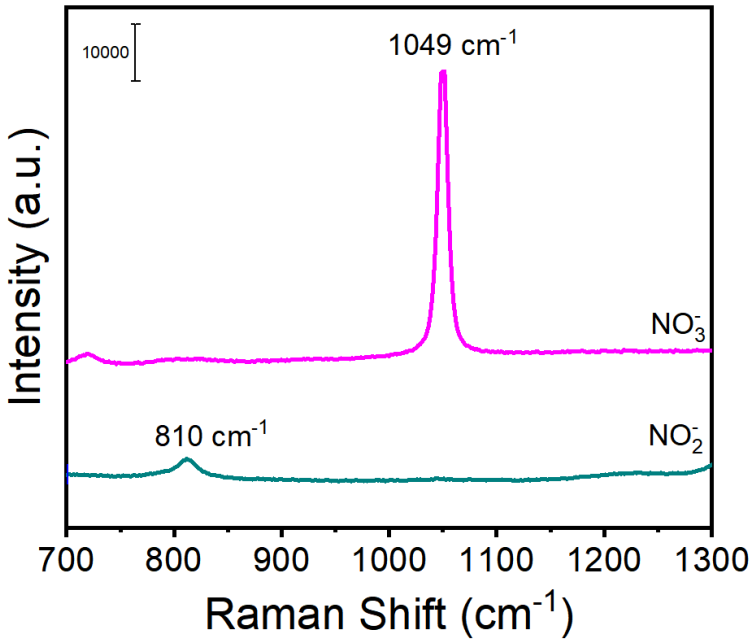


**Supplementary Fig. 39. Raman spectra of 1 M $KNO_3$ and 1 M $KNO_2$ electrolyte.** The ratio of the integrated area of $NO_2^-$ to $NO_3^-$ was determined as a correction factor (0.128) to calculate the local concentration of $NO_2^-$.

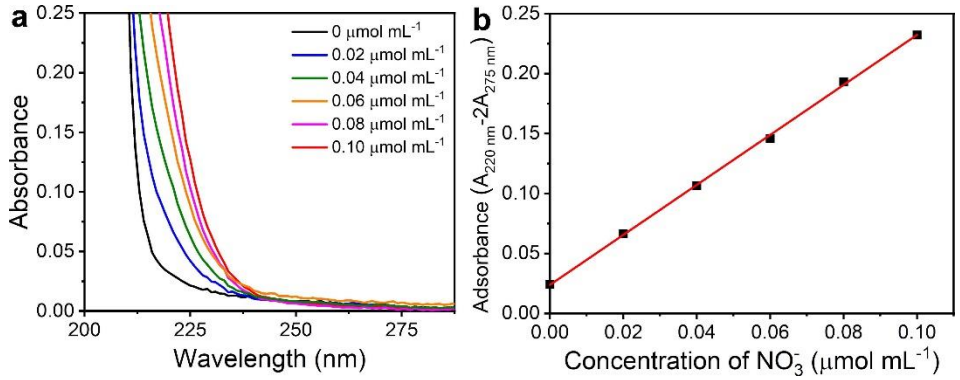


**Supplementary Fig. 40. Determination of $NO_3^-$.** (a) UV-vis curves and (b) concentration-absorbance curve of $NO_3^-$ solution with a series of standard concentrations. The standard curve showed linear relation of absorbance with $NO_3^-$ concentration ($y = 2.084\ x + 0.024$, $R^2 = 0.9992$).

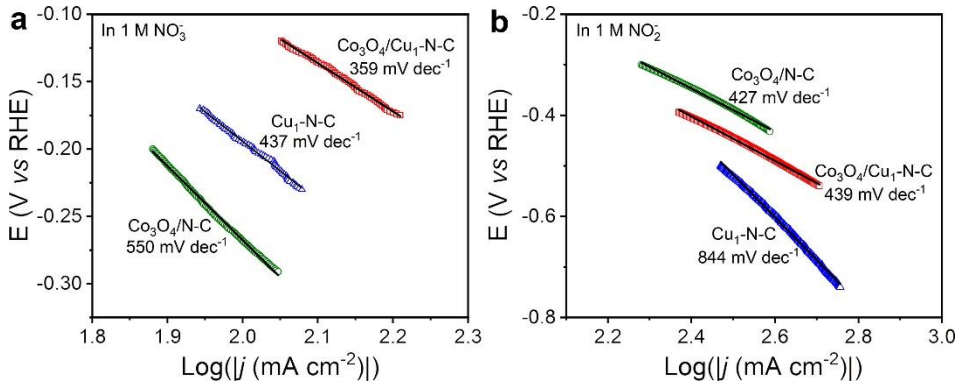


**Supplementary Fig. 41. Tafel slopes of $Cu_1$-N-C, $Co_3O_4$/N-C, and $Co_3O_4$/$Cu_1$-N-C in (a) $NO_3^-$ and (b) 1 M $NO_2^-$.** In 1 M $NO_3^-$, the Tafel slopes of $Co_3O_4$/$Cu_1$-N-C was smaller than those of $Co_3O_4$/N-C and $Cu_1$-N-C. This result implies that $Co_3O_4$/N-C facilitated the kinetics of $NO_3^-$ reduction. In the case of 1 M $NO_2^-$, the Tafel slopes of $Co_3O_4$/$Cu_1$-N-C was close to that of $Co_3O_4$/N-C but lower than that of $Cu_1$-N-C, indicating a faster $NO_2^-$ reduction kinetics on $Co_3O_4$ species. As such, the combination of $Co_3O_4$ with $Cu_1$-N-C also promoted the kinetics of the subsequent $NO_2^-$ reduction.

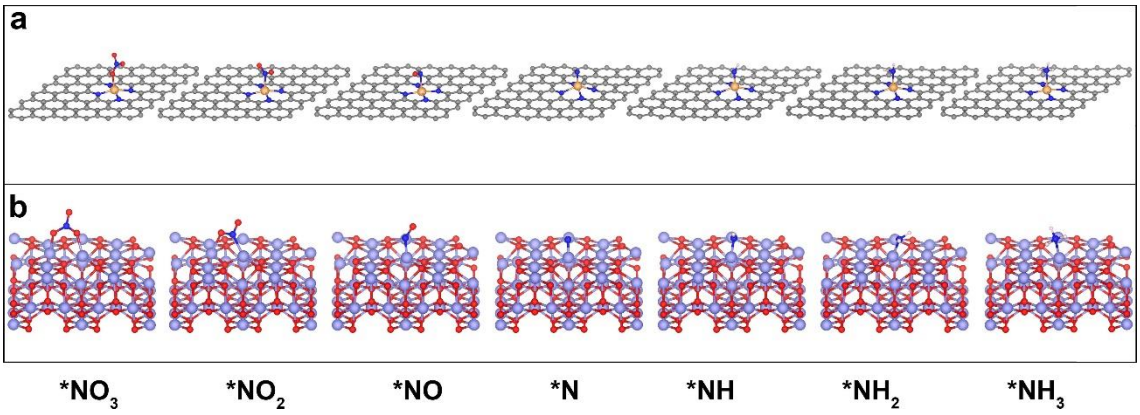


**Supplementary Fig. 42. The structure models of intermediates on (a) $CuN_4$ and (b) $Co_3O_4$ (100) slabs.** The gray, blue, red, white, yellow, and purple spheres represent C, N, O, H, Cu, and Co atoms, respectively.

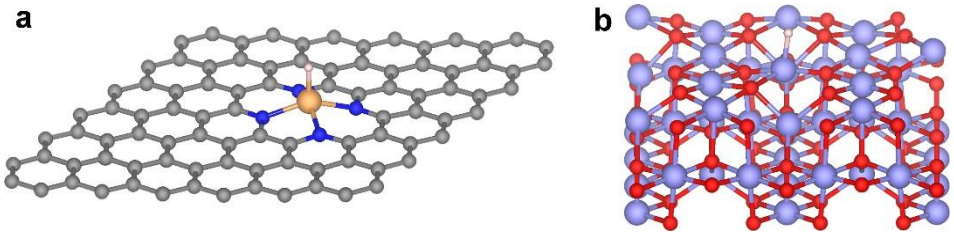


**Supplementary Fig. 43. The structure models of *H adsorbed on (a) $CuN_4$ and (b) $Co_3O_4$ (100) slabs.** The gray, blue, red, white, yellow, and purple spheres represent C, N, O, H, Cu, and Co atoms, respectively.

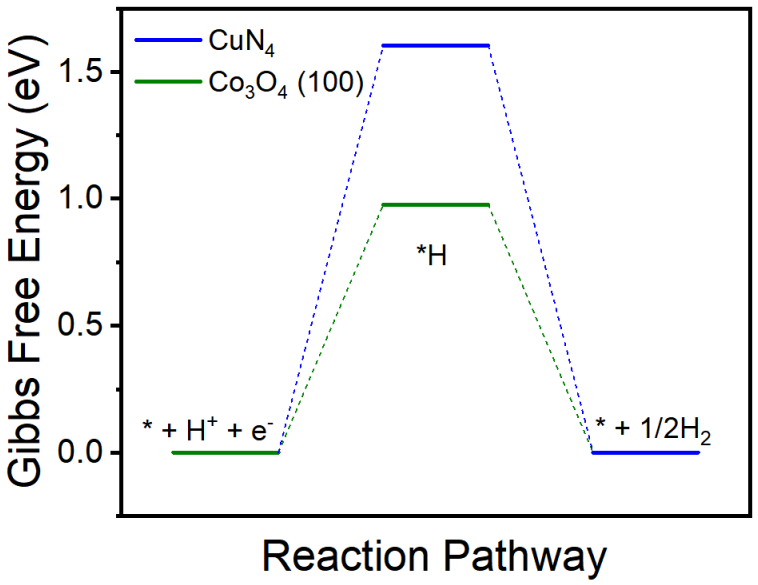


**Supplementary Fig. 44. Gibbs free energy diagrams of the *H adsorption on $CuN_4$ and $Co_3O_4$ (100).**

**References**


1 Wang, Y. *et al.* Enhanced nitrate-to-ammonia activity on copper-nickel alloys via tuning of intermediate adsorption. *J. Am. Chem. Soc.* **142**, 5702-5708, (2020).

2 He, W. *et al.* Splicing the active phases of copper/cobalt-based catalysts achieves high-rate tandem electroreduction of nitrate to ammonia. *Nat. Commun.* **13**, 1129, (2022).

3 Liu, H. *et al.* Efficient electrochemical nitrate reduction to ammonia with copper-supported rhodium cluster and single-atom catalysts. *Angew. Chem. Int. Ed.* **61**, e202202556, (2022).

4 Yang, J. *et al.* Potential-driven restructuring of cu single atoms to nanoparticles for boosting the electrochemical reduction of nitrate to ammonia. *J. Am. Chem. Soc.* **144**, 12062-12071, (2022).

5 Wang, J. *et al.* Electrocatalytic reduction of nitrate to ammonia on low-cost ultrathin $coo_x$ nanosheets. *ACS Catal.* **11**, 15135-15140, (2021).

6 Chen, F. Y. *et al.* Efficient conversion of low-concentration nitrate sources into ammonia on a ru-dispersed cu nanowire electrocatalyst. *Nat. Nanotechnol.* **17**, 759-767, (2022).

7 Gao, P. *et al.* Schottky barrier-induced surface electric field boosts universal reduction of nox- in water to ammonia. *Angew. Chem. Int. Ed.* **60**, 20711-20716, (2021).

8 McEnaney, J. M. *et al.* Electrolyte engineering for efficient electrochemical nitrate reduction to ammonia on a titanium electrode. *ACS Sustain. Chem. Eng.* **8**, 2672-2681, (2020).

9 Harmon, N. J. *et al.* Intrinsic catalytic activity of carbon nanotubes for electrochemical nitrate reduction. *ACS Catal.* **12**, 9135-9142, (2022).

10 Wu, Z.-Y. *et al.* Electrochemical ammonia synthesis via nitrate reduction on fe single atom catalyst. *Nat. Commun.* **12**, 2870, (2021).

11 Jia, Y. *et al.* Efficient nitrate-to-ammonia electroreduction at cobalt phosphide nanoshuttles. *ACS Appl. Mater. Interfaces* **13**, 45521-45527, (2021).

12 Li, J. *et al.* Efficient ammonia electrosynthesis from nitrate on strained ruthenium nanoclusters. *J. Am. Chem. Soc.* **142**, 7036-7046, (2020).

13 Fan, K. *et al.* Active hydrogen boosts electrochemical nitrate reduction to ammonia. *Nat. Commun.* **13**, 7958, (2022).

14 Zhu, J.-Y. *et al.* Iridium nanotubes as bifunctional electrocatalysts for oxygen evolution and nitrate reduction reactions. *ACS Appl. Mat. Interfaces* **12**, 14064-14070, (2020).

15 Zhang, N. *et al.* Governing interlayer strain in bismuth nanocrystals for efficient ammonia

electrosynthesis from nitrate reduction. *ACS Nano* **16**, 4795-4804, (2022).

16 Gao, Q. *et al*. Synthesis of core/shell nanocrystals with ordered intermetallic single-atom alloy layers for nitrate electroreduction to ammonia. *Nat. Synth.* **2**, 624-623 (2023).